# Semiclassical approach for solving the time-dependent Schrödinger equation in spatially inhomogeneous electromagnetic pulses

Jianxiong Li and Uwe Thumm

Phys. Rev. A **101**, 013411 — Published 9 January 2020
DOI: 10.1103/PhysRevA.101.013411

# A semi-classical approach for solving the time-dependent Schrödinger equation in spatially inhomogeneous electromagnetic pulses

Jianxiong Li and Uwe Thumm
*Department of Physics, Kansas State University, Manhattan, Kansas 66506, USA*

(Dated: December 11, 2019)

To solve the time-dependent Schrödinger equation in spatially inhomogeneous pulses of electromagnetic radiation, we propose an iterative semi-classical complex trajectory approach. In numerical applications, we validate this method against *ab initio* numerical solutions by scrutinizing (a) electronic states in combined Coulomb and spatially homogeneous laser fields and (b) streaked photoemission from hydrogen atoms and plasmonic gold nanospheres. In comparison with streaked photoemission calculations performed in strong-field approximation, we demonstrate the improved reconstruction of the spatially inhomogeneous induced plasmonic infrared field near a nanoparticle surface from streaked photoemission spectra.

## I. INTRODUCTION

The exposure of gaseous atomic, mesoscopic, and solid targets to incident pulses of electromagnetic radiation of sufficiently high photon energy or intensity leads to the emission of photoelectrons [1]. For more than a century, photoelectron spectroscopy has very successfully exploited this phenomenon and has long become established as one of the most prolific techniques for unraveling the *static* electronic structure of matter by examining the kinetic-energy or momentum distribution of emitted photoelectrons. More recently, starting in the 21st century, advances in ultrafast laser technology started to extend photoemission spectroscopy into the time domain [2–4]. Importantly, the development of attosecond streaking [5, 6] and interferometric [7–9] photoelectron spectroscopy enabled the observation of electron dynamics at the natural time scale of the electron motion in matter (attoseconds, 1 as $= 10^{-18}$ s). This was demonstrated in proof-of-principle experiments for gaseous atomic [10–16] and molecular [17–19] targets. Attosecond time-resolved photoemission spectroscopy is currently being extended to complex targets [6, 20], such as nanostructures and nanoparticles [21–28], and solid surfaces [9, 29–36], making it possible to examine, for example, the dynamics of photoemission from a surface on an absolute time scale [37] and suggesting, for example, the time-resolved observation of the collective motion of electrons (plasmons) in condensed-matter systems [38–40].

In combination with advances in nanotechnology, allowing the production of plasmonic nanostructures with increasing efficiency at the nm length scale, attosecond photoemission spectroscopy has started to progress towards the spatiotemporal imaging of electron dynamics in complex targets, approaching the atomic length and time scales (nm and attoseconds) [20, 21, 25–28, 31, 41, 42]. Photoemission spectroscopy therefore holds promise to become a powerful tool for examining nm-attosecond scale processes that are operative in plasmonically enhanced photocatalysis [43], light harvesting [44], surface-enhanced Raman spectroscopy [45], biomedical and chemical sensing [46], tumor detection and treatment [47], and ultrafast electro-optical switching [48]. The concurrent development and provision of large-scale light sources, capable of producing intense ultrashort pulses in the extreme ultraviolet (XUV) to X-ray spectral range at several leading laboratories in Europe, the United Stated, and Japan [49, 50], promises to further boost the value of spatiotemporally resolved electron spectroscopy as a tool for imaging electronic dynamics within a wide array of basic and applied research projects.

Being able to take advantage of the full potential offered by current and emerging atomic scale photoelectron imaging techniques relies on theoretical and numerical modeling. This is true for comparatively simple atoms in the gas phase, and for complex nanostructured targets additional theoretical challenges arise [6, 20]. While for atomic photoionization by visible and near UV light, the size of the target is small compared to the wavelength of the incident light pulse, this is no longer true for X-ray ionization, leading to the well-know breakdown of the dipole approximation [51, 52]. Furthermore, for nanoparticles [22–28], (nanostructured) surfaces [36, 53–55], and layered structures [35, 36, 42, 56], not only the comparability of the wavelength and structure size requires careful quantum-mechanical modeling beyond the dipole approximation, but also the target's spatially inhomogeneous dielectric response to the incident light pulse [54, 55]. Most numerical models for streaked and interferometric photoemission from atoms are based on the so-called 'strong-field approximation (SFA)' [6]. The SFA builds on the assumption that photo-emitted electrons are solely exposed to *spatially homogeneous* external fields. It discards all other interactions photo-released electrons may be subject to (e.g., with the residual parent ion) and cannot accommodate spatially inhomogeneous final-state interactions.

While the SFA was shown to deteriorate for lower photoelectron energies [57], it completely looses its applicability for complex targets as screening and plasmonic effects expose photoelectrons to *inhomogeneous* net electromagnetic fields [6, 38, 54, 55]. The convenient use of analytically known so-called 'Volkov wavefunctions' for the photoelectron's motion in homogeneous electromagnetic fields [58] is no longer acceptable, since dielectric response effects entail screening length and induced plasmonic fields at the nm length scale [22, 24–28, 36, 38]. Thus, the numerical modeling of photoemission from complex targets with morphologies or plasmonic response lengths at the nm scale by intense short wavelength pulses (made increasingly available at new (X)FEL light sources [49, 50]), necessitates photoemission models beyond the SFA.

To this effect we previously employed heuristically generalized Volkov states to model photoemission from bare and adsorbate-covered metal surfaces [35, 36, 54, 55] and plasmonic nanoparticles [22, 26, 28]. While this allowed us to numerically model streaked [42, 54, 55, 59] and interferometric photoemission spectra from surfaces [35, 36], in fair to good agreement with experimental data, and to reconstruct plasmonic fields near gold nanospheres [28], a systematic mathematical solution of the time-dependent Schrödinger (TDSE) for a single active electron exposed to inhomogeneous external fields remains to be explored. We here discuss a semiclassical model for obtaining such solutions. While being approximate, our complex-phase Wentzel-Kramer-Brillouin (WKB)-type approach lends itself to systematic iterative refinement. Our proposed method, termed ACCTIVE (Action Calculation by Classical Trajectory Integration in Varying Electromagnetic fields), employs complex classical trajectories to solve the TDSE in the presence of spatially inhomogeneous electromagnetic pulses that are represented by time-dependent inhomogeneous scalar and vector potentials. Our approach is inspired by the semiclassical complex-trajectory method for solving the TDSE with time-independent scalar interactions of Boiron and Lombardi [60] and its adaptation to time-dependent scalar interactions by Goldfarb, Schiff, and Tannor [61].

Following the mathematical formulation of ACCTIVE in Sec. II, we validate this method by discussing five examples in Sec. III. We first compare ACCTIVE calculations with *ab initio* numerical solutions by scrutinizing electronic states in a (i) homogeneous laser field, (ii) Coulomb field, and (iii) combination of laser and Coulomb fields. Next, we apply ACCTIVE to streaked photoemission from (iv) hydrogen atoms and (v) plasmonic nanoparticles. In the application to Au nanospheres, we examine final states for the simultaneous interaction of the photoelectron with the spatially inhomogeneous plasmonically enhanced field induced by the streaking infrared (IR) laser pulse and demonstrate the improved reconstruction of the induced nanoplasmonic IR field from streaked photoemission spectra. Section IV contains our summary. In four appendices we prove the gauge invariance of the ACCTIVE method (Appendix A) and add details of our calculations within ACCTIVE of Volkov wavefunctions (Appendix B) and Coulomb wavefunctions (Appendix C), and additional comments on streaked photoemission from Au nanospheres (Appendix D).

## II. THEORY

We seek approximate solutions of the TDSE for a particle of (effective) mass $m$ and charge $q$ in an inhomogeneous time-dependent electro-magnetic field given by the scalar and vector potentials $\phi(\mathbf{r},t)$ and $\mathbf{A}(\mathbf{r},t)$ and an additional scalar potential $V(\mathbf{r},t)$,

$$i\hbar\frac{\partial}{\partial t}\Psi(\mathbf{r},t) = \left\{\frac{1}{2m}\Big[i\hbar\nabla + q\mathbf{A}(\mathbf{r},t)\Big]^2 + \varphi(\mathbf{r},t)\right\}\Psi(\mathbf{r},t), \tag{1}$$

where $\varphi(\mathbf{r},t) = q\phi(\mathbf{r},t) + V(\mathbf{r},t)$ and $V(\mathbf{r},t)$ is any scalar potential. Representing the wavefunction in eikonal form, $\Psi(\mathbf{r},t) = e^{iS(\mathbf{r},t)/\hbar}$, Eq. (1) can be rewritten in terms of the complex-valued quantum-mechanical action $S(\mathbf{r},t)$,

$$\begin{aligned}\frac{\partial}{\partial t}S(\mathbf{r},t) + \frac{1}{2m}\Big[\nabla S(\mathbf{r},t) - q\mathbf{A}(\mathbf{r},t)\Big]^2 + \varphi(\mathbf{r},t)\\ = \frac{i\hbar}{2m}\nabla\cdot\Big[\nabla S(\mathbf{r},t) - q\mathbf{A}(\mathbf{r},t)\Big].\end{aligned} \tag{2}$$

Expanding the action in powers of $\hbar$ [60, 61],

$$S(\mathbf{r},t) = \sum_{n=0}^{\infty}\hbar^n S_n(\mathbf{r},t), \tag{3}$$

substituting Eq. (3) into Eq. (2), and comparing terms of equal order, results in the set of coupled partial differential equations

$$\frac{\partial}{\partial t}S_0(\mathbf{r},t) + \frac{\big[\nabla S_0(\mathbf{r},t) - q\mathbf{A}(\mathbf{r},t)\big]^2}{2m} + \varphi(\mathbf{r},t) = 0 \tag{4a}$$

$$\begin{aligned}\frac{\partial}{\partial t}S_1(\mathbf{r},t) + \left[\frac{\nabla S_0(\mathbf{r},t) - q\mathbf{A}(\mathbf{r},t)}{m}\right]\cdot\nabla S_1(\mathbf{r},t)\\ = \frac{i}{2}\nabla\cdot\left[\frac{\nabla S_0(\mathbf{r},t) - q\mathbf{A}(\mathbf{r},t)}{m}\right]\end{aligned} \tag{4b}$$

$$\begin{aligned}\frac{\partial}{\partial t}S_n(\mathbf{r},t) + \left[\frac{\nabla S_0(\mathbf{r},t) - q\mathbf{A}(\mathbf{r},t)}{m}\right]\cdot\nabla S_n(\mathbf{r},t)\\ = -\frac{1}{2m}\sum_{j=1}^{n-1}\nabla S_j(\mathbf{r},t)\cdot\nabla S_{n-j}(\mathbf{r},t)\\ + \frac{i}{2m}\nabla^2 S_{n-1}(\mathbf{r},t) \qquad (n \geq 2),\end{aligned} \tag{4c}$$

where the lowest-order contribution $S_0(\mathbf{r},t)$ is the classical action of a charged particle moving in the electromagnetic field

$$\begin{cases}\mathbf{E}(\mathbf{r},t) &= -\nabla\varphi(\mathbf{r},t)/q - \partial\mathbf{A}(\mathbf{r},t)/\partial t\\ \mathbf{B}(\mathbf{r},t) &= \nabla\times\mathbf{A}(\mathbf{r},t).\end{cases} \tag{5}$$

With regard to the ongoing discussion about the gauge (in)variance of approximate solutions of the TDSE for intense-external field interactions with matter (see, e.g., [52, 62, 63] and refs. therein), we point out that Eqs. (4) are form invariant under gauge transformations

$$\begin{cases} \mathbf{A} & \mapsto \quad \mathbf{A}' = \mathbf{A} + \nabla f(\mathbf{r},t) \\ \varphi & \mapsto \quad \varphi' = \varphi - q\frac{\partial}{\partial t} f(\mathbf{r},t), \end{cases} \tag{6}$$

defined in terms of arbitrary differentiable functions $f(\mathbf{r},t)$, that leave the external fields $\mathbf{E}(\mathbf{r},t)$ and $\mathbf{B}(\mathbf{r},t)$ unchanged. This invariance requires the classical action to transform according to

$$\begin{cases} S_0(\mathbf{r},t) & \mapsto \quad S_0'(\mathbf{r},t) = S_0(\mathbf{r},t) + qf(\mathbf{r},t) \\ S_n(\mathbf{r},t) & \mapsto \quad S_n'(\mathbf{r},t) = S_n(\mathbf{r},t) \qquad (n \geq 1), \end{cases} \tag{7}$$

in agreement with the known unitary local gauge transformation of the wave function $\Psi(\mathbf{r},t)$ according to $\Psi(\mathbf{r},t) \mapsto \Psi'(\mathbf{r},t) = e^{iqf(\mathbf{r},t)/\hbar}\Psi(\mathbf{r},t)$ [51, 63]. Here, the complex phase $qf(\mathbf{r},t)/\hbar$ appears only in $S_0(\mathbf{r},t)$. For further comments see Appendix A.

Solving the classical Hamilton-Jacobi equation (HJE) Eq. (4a) leads to Newton's Second Law,

$$\frac{d}{dt}\mathbf{v}(\mathbf{r},t) = \frac{q}{m}\Big[\mathbf{E}(\mathbf{r},t) + \mathbf{v}(\mathbf{r},t) \times \mathbf{B}(\mathbf{r},t)\Big], \tag{8}$$

where the classical velocity field $\mathbf{v}(\mathbf{r},t)$ and kinetic momentum,

$$\mathbf{p}(\mathbf{r},t) \equiv m\mathbf{v}(\mathbf{r},t) \equiv \nabla S_0(\mathbf{r},t) - q\mathbf{A}(\mathbf{r},t), \tag{9}$$

are given in terms of the gauge invariant canonical momentum $\nabla S_0(\mathbf{r},t)$ [64] (See Appendix A). The combination of the HJE (4a) and Eq. (9) provides the Lagrangian $L\big[\mathbf{r},\mathbf{v}(\mathbf{r},t),t\big]$ as a total time differential of $S_0(\mathbf{r},t)$,

$$\begin{aligned} \frac{d}{dt}S_0(\mathbf{r},t) &= L\big[\mathbf{r},\mathbf{v}(\mathbf{r},t),t\big] \\ &= \frac{1}{2}m\mathbf{v}^2(\mathbf{r},t) + q\mathbf{v}(\mathbf{r},t)\cdot\mathbf{A}(\mathbf{r},t) - \varphi(\mathbf{r},t). \end{aligned} \tag{10}$$

Similarly, by substituting Eq. (9) into Eqs. (4b) and (12), we find the total time derivatives of the first-order contribution to $S(\mathbf{r},t)$,

$$\frac{d}{dt}S_1(\mathbf{r},t) = \frac{i}{2}\nabla\cdot\mathbf{v}(\mathbf{r},t), \tag{11}$$

and of all higher order terms,

$$\begin{aligned} \frac{d}{dt}S_n(\mathbf{r},t) = &-\frac{1}{2m}\sum_{j=1}^{n-1}\nabla S_j(\mathbf{r},t)\cdot\nabla S_{n-j}(\mathbf{r},t) \\ &+ \frac{i}{2m}\nabla^2 S_{n-1}(\mathbf{r},t) \qquad (n \geq 2). \end{aligned} \tag{12}$$

Approximate solutions to $S(\mathbf{r},t)$ can be obtained by iteration of Eq. (12), after integrating the total time derivatives in Eqs. (10), (11), and (12) along classical trajectories $\tilde{\mathbf{r}}(t)$ that are defined by

$$\frac{d}{dt}\tilde{\mathbf{r}}(t) \equiv \mathbf{v}\big[\tilde{\mathbf{r}}(t),t\big] \tag{13}$$

with respect to a reference time (integration constant) $t_r$. The wavefunction at $t_r$, $\Psi_r(\mathbf{r}) = \Psi(\mathbf{r},t_r)$, provides initial ($t_r \ll 0$) or asymptotic ($t_r \gg 0$) conditions in terms of the action

$$S(\mathbf{r},t_r) = -i\hbar\ln[\Psi_r(\mathbf{r})] \tag{14}$$

and the velocity field

$$\begin{aligned} \mathbf{v}(\mathbf{r},t_r) &= -\frac{1}{m}\nabla S_0(\mathbf{r},t_r) - \frac{q}{m}\mathbf{A}(\mathbf{r},t_r) \\ &\approx -\frac{1}{m}\nabla S(\mathbf{r},t_r) - \frac{q}{m}\mathbf{A}(\mathbf{r},t_r) \\ &= -\frac{i\hbar\nabla\Psi_r(\mathbf{r})}{m\Psi_r(\mathbf{r})} - \frac{q}{m}\mathbf{A}(\mathbf{r},t_r). \end{aligned} \tag{15}$$

The semiclassical solution of Eqs. (10), (11), and (12) requires an appropriate classical trajectory $\tilde{\mathbf{r}}(t')$ - for any given 'current' event $(\mathbf{r},t)$ - that connects the 'current' coordinate and velocity,

$$\mathbf{r} = \tilde{\mathbf{r}}(t), \qquad \mathbf{v} = \frac{d\tilde{\mathbf{r}}(t')}{dt'}\bigg|_t, \tag{16}$$

to the proper coordinate and velocity at $t_r$,

$$\mathbf{r}_r = \tilde{\mathbf{r}}(t_r), \tag{17a}$$

$$\mathbf{v}_r = \frac{d\tilde{\mathbf{r}}(t')}{dt'}\bigg|_{t_r} = -\frac{i\hbar\nabla\Psi_r(\mathbf{r}_r)}{m\Psi_r(\mathbf{r}_r)} - \frac{q}{m}\mathbf{A}(\mathbf{r}_r,t_r). \tag{17b}$$

The known quantities in Eqs. (16) and (17) are $\mathbf{r}$, $t$, and $t_r$, while $\mathbf{v}$, $\mathbf{r}_r$, and $\mathbf{v}_r$ are to be determined. To numerically calculate the undetermined quantities, we employ a shooting method, starting with a 'trial' velocity $\mathbf{v}^{trial}$ at position $\mathbf{r}$ and time $t$. Propagating $\mathbf{r}$ to the reference time according to Eq. (8) results in $\mathbf{r}_r^{trial} = \tilde{\mathbf{r}}^{trial}(t_r)$ and $\mathbf{v}_r^{trial} = d\tilde{\mathbf{r}}^{trial}(t')/dt' \mid_{t_r}$ (Fig. 1).

The velocity field $\mathbf{v}$ that satisfies Eq. (8) can now be found numerically by determining the roots of the function

$$f(\mathbf{v}^{trial}) = \Big| \, \mathbf{v}_r^{trial} + \frac{i\hbar\nabla\Psi_r(\mathbf{r}_r^{trial})}{m\Psi_r(\mathbf{r}_r^{trial})} + \frac{q}{m}\mathbf{A}(\mathbf{r}_r^{trial},t_r) \, \Big| \tag{18}$$

for an appropriate range of start trial velocities. In our numerical applications this is accomplished by an efficient multi-dimensional quasi-Newton root-finding algorithm (Broyden's method) [65, 66]. Once the correct trajectories $\tilde{\mathbf{r}}(t')$ are determined by finding the roots of Eq. (18), the actions in Eqs. (10), (11), and (12) are integrated along these trajectories and composed - by truncating Eq. (3) - into an approximate solution of Eq. (1).

Since each term $S_n(\mathbf{r},t)$ in Eq. (3) depends only on terms of lower orders, ACCTIVE enables, in principle, the systematic iterative refinement of approximate solutions of Eq. (1) by including successively higher orders $n$. The iteration is started with $S_0(\mathbf{r},t)$, which is determined by the velocity field $\mathbf{v}(\mathbf{r},t)$, and continued by integrating Eqs. (11) and (12).

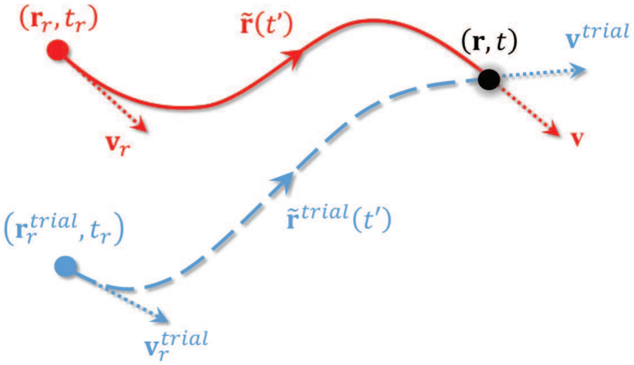

Figure 1. (Color online) Illustration of the shooting method used for determining classical trajectories. For any given event $(\mathbf{r}, t)$ and a predetermined reference time $t_r$, trajectories are classically propagated from trial points in phase space, $(\mathbf{r}, \mathbf{v}^{trial})$, at time $t$ along trial trajectories $\tilde{\mathbf{r}}^{trial}(t')$. The velocity field $\mathbf{v}$ and appropriate trajectory $\tilde{\mathbf{r}}(t')$ are determined by iterating the trial velocity $\mathbf{v}^{trial}$ in order to find the roots of $f(\mathbf{v}^{trial})$ in Eq. (18).

In the numerical examples discussed in Sec. III below, we find that retaining only the zero'th and first-order terms, $S_0(\mathbf{r}, t)$ and $S_1(\mathbf{r}, t)$, provides sufficiently accurate and physically meaningful solutions at modest numerical expense. Thus, according to Eqs. (10) and (11), we apply

$$\begin{aligned}\Psi(\mathbf{r}, t) &\approx \exp\left\{iS_0(\mathbf{r}, t)/\hbar + iS_1(\mathbf{r}, t)\right\} \\ &= e^{iS(\mathbf{r}_r, t_r)/\hbar} \exp\left\{ -\frac{1}{2}\int_{t_r}^{t} \nabla\cdot\mathbf{v}\Big(\tilde{\mathbf{r}}(t'), t'\Big)dt' \right. \\ &\left. \quad + \frac{i}{\hbar}\int_{t_r}^{t} L\Big[\tilde{\mathbf{r}}(t'), \mathbf{v}\Big(\tilde{\mathbf{r}}(t'), t'\Big), t'\Big]dt' \right\}. \qquad (19)\end{aligned}$$

For real classical trajectories and potentials, the integral of $S_0(\mathbf{r}, t)$ is real, representing a local phase factor, while $S_1(\mathbf{r}, t)$ is purely imaginary and defines the wavefunction amplitude, as in the standard WKB approach [51]. The quantum-mechanical probability density $\rho(\mathbf{r}, t)$ then satisfies the continuity equation,

$$\frac{d\rho(\mathbf{r}, t)}{dt} = \frac{d}{dt}|\Psi(\mathbf{r}, t)|^2 = -\rho(\mathbf{r}, t)\nabla\cdot\mathbf{v}(\mathbf{r}, t), \qquad (20)$$

for the classical probability flux $\rho(\mathbf{r}, t)\,\mathbf{v}(\mathbf{r}, t)$ [67].

## III. EXAMPLES

We validate the ACCTIVE method by discussing five applications to electron wavefunctions in Coulomb and laser fields.

### A. Volkov wavefunction

For the simple example of an electron in a time-dependent, spatially homogeneous laser field, the potentials in Eq. (1) and reference wavefunction are (in the Coulomb electromagnetic gauge [51])

$$\mathbf{A}(\mathbf{r}, t) = \mathbf{A}(t), \quad \varphi(\mathbf{r}, t) = 0, \quad \Psi_r(\mathbf{r}) = e^{i\mathbf{p}\cdot\mathbf{r}/\hbar}, \qquad (21)$$

and the first-order wavefunction in Eq. (19) reproduces the well-known analytical Volkov solution [58],

$$\Psi^V(\mathbf{r}, t) = \exp\left\{\frac{i\;\mathbf{p}\cdot\mathbf{r}}{\hbar} - \frac{i}{2m\hbar}\int_{t_r}^{t}\left[\mathbf{p} - q\mathbf{A}(t')\right]^2 dt'\right\}. \qquad (22)$$

For details of the derivation of Eq. (22) within ACCTIVE see Appendix B.

### B. Coulomb wavefunction

As a second simple example and limiting case, we consider an unbound electron in the Coulomb field of a proton. In this case the potentials in Eq. (1) are

$$\mathbf{A}(\mathbf{r}, t) = 0, \quad \varphi(\mathbf{r}, t) = -k_e\frac{e^2}{r}, \qquad (23)$$

where $e$ is the elementary charge and $k_e$ the electrostatic constant. Assuming outgoing-wave boundary conditions, we define the reference wavefunction at a sufficiently large reference time $t_r$ as the 'outgoing' Coulomb wave

$$\Psi_r(\mathbf{r}, t_r) \xrightarrow{t_r\to\infty,\ z\to+\infty} e^{i\left(kz - \frac{\hbar k^2}{2m}t_r\right)}. \qquad (24)$$

Here $\mathbf{r} = (x, y, z)$ and $p = \hbar k > 0$ is the final electron momentum. In this case the TDSE is solved exactly by the well-known Coulomb wavefunction

$$\Psi_k^C(\mathbf{r}, t) = \frac{e^{\frac{\pi}{2k}}\Gamma(1 - i/k)}{(2\pi)^{3/2}}\,{}_1F_1(i/k, 1, ikr - ikz)e^{i\left(kz - \frac{\hbar k^2}{2m}t\right)} \qquad (25)$$

in terms of the confluent hypergeometric function ${}_1F_1$. Note that for finite distances from the $z$-axis (i.e., for finite coordinates $x$ and $y$), the asymptotic form of the Coulomb continuum wavefunction for $z \to +\infty$ is just a plane wave (without a logarithmic phase term) [51, 68].

Applying ACCTIVE to the outgoing-wave Coulomb problem, $t_r$ must be chosen sufficiently long after $t$, so that each classical trajectory $\tilde{\mathbf{r}}(t')$ propagates far enough towards the $z \to +\infty$ asymptotic limit for the reference velocity to become

$$\mathbf{v}_r \xrightarrow{t_r\to\infty,\ z\to+\infty} \hat{\mathbf{z}}p/m, \qquad (26)$$

in compliance with Eq. (17b). In this and for the following numerical example, we use as reference velocity the initial trial velocity for points of the spatial numerical grid that are sufficiently far away from the Coulomb singularity at the origin. The correct 'current' velocities, $\mathbf{v}(\mathbf{r}, t)$ at the most distant coordinates are subsequently used as trial velocities at the nearest neighbor spatial grid points. This scheme is continued until classical trajectories for the entire spatiotemporal numerical grid are

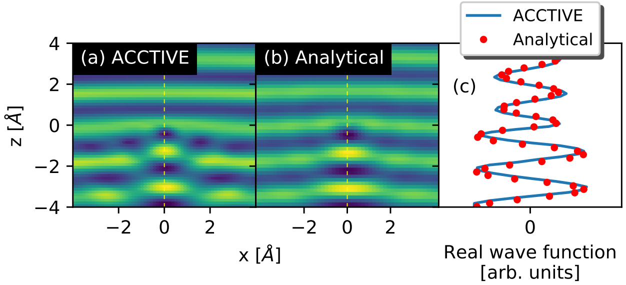

Figure 2. (Color online) Real part of an unbound Coulomb wavefunction , subject to the boundary condition given by an outgoing wave propagating along the $z$-axis. (a) Numerically calculated semi-classical 1st order ACCTIVE wavefunction. (b) Analytical Coulomb wavefunction in the $y = 0$ plane. (c) Real part of the wavefunctions in (a) and (b) along the $z$-axis for $x = y = 0$.

calculated. Further details of the numerical calculation of Coulomb wavefunctions within ACCTIVE are given in Appendix C.

Figure 2 shows the very good agreement between the numerically calculated 1st order ACCTIVE wavefunction (19) and the analytical Coulomb wavefunction (25) for a final electron kinetic energy of $p^2/2m = 50$ eV. The color/gray scale represents the real part of the wavefunction in the $x - z$ plane. Figures 2(a) and 2(b) show the same scattering pattern. Good quantitative agreement of the 1st order ACCTIVE wavefunction and the analytical Coulomb wavefunction is demonstrated in Fig. 2(c).

### C. Coulomb-Volkov wavefunction

A more challenging third example is given by the motion of an electron under the combined influence of a point charge (proton), located at the coordinate origin, and a spatially homogeneous laser pulse, subject to the boundary condition Eq. (24). In this case, the potentials in Eq. (1) are (in Coulomb gauge [51])

$$\mathbf{A}(\mathbf{r}, t) = \mathbf{A}(t), \quad \varphi(\mathbf{r}, t) = -k_e \frac{e^2}{r}. \tag{27}$$

Considering a laser pulse of finite duration, $t_r$ must be chosen such that the laser electric field vanishes at $t_r$. This combination of the two previous examples in Secs. III A and III B constitutes the Coulomb-Volkov problem, for which merely approximate solutions [69–72], but no analytical wavefunction are known. We assume a laser pulse with 15 eV central photon energy, a cosine-square temporal intensity envelope with a pulse length of 0.5 fs full width at half intensity maximum (FWHIM), and $3 \times 10^{15}$ W/cm$^2$ peak intensity. At time $t = 0$, the temporal pulse profile is centered at $z = 0$. We enforce the outgoing-wave boundary condition (24) for an asymptotic photoelectron kinetic energy of $p^2/2m = 50$ eV. This energy is reached at a sufficiently large distance of the outgoing electron from the proton and long after the pulse has vanished.

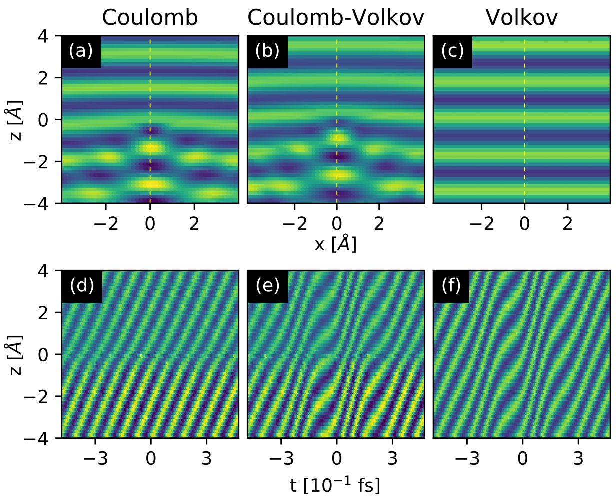

Figure 3. (Color online) Real parts of (a,d) Coulomb, (b,e) ACCTIVE-calculated Coulomb-Volkov, and (c,f) Volkov wavefunctions in the $y = 0$ plane. (a-c) Snapshots at time $t = 0$, when the laser-pulse center is at $z = 0$. (d-f) Time evolution along the $z$-axis.

In Fig. 3 we compare the ACCTIVE-calculated Coulomb-Volkov wavefunction with Coulomb and Volkov wavefunctions for identical outgoing-wave boundary condition and 50 eV asymptotic photoelectron kinetic energy. The Coulomb and Volkov wavefunctions are given for a positive elementary charge and the same laser parameters as the Coulomb-Volkov wave, respectively. The color/gray scale represents the real part of the wavefunctions. We determined all numerical parameters (numerical grid size, spacing and propagation time step) to ensure convergence of the wavefunctions.

Figures 3(a), 3(b), and 3(c), display snapshots at time $t = 0$ of the Coulomb, ACCTIVE-calculated Coulomb-Volkov, and Volkov wavefunctions, respectively. The Coulomb-Volkov wavefunction shows a similar (inverse) Coulomb scattering pattern for the incident wave ($z < 0$) as the Coulomb wave. Its outgoing part ($z > 0$) closely matches the phase of the Volkov wave. On the other hand, the time-dependent evolution of the Coulomb-Volkov wavefunction in the $y = 0$ plane in Fig. 3(e) shows laser-induced wavefront distortions - similar to the Volkov wave in Fig. 3(f). The time evolution of the ACCTIVE-calculated Coulomb-Volkov wavefunction reveals the acceleration of the incoming and deceleration of the outgoing wave near the proton at $z = 0$ of the pure Coulomb wave in Fig. 3(d). An animated version of this wavefunction comparison can be found in the Supplemental Material [73].

### D. Streaked photoemission from hydrogen atoms

As a fourth example, we employ ACCTIVE final-state wavefunctions to calculate IR-streaked XUV photoelectron spectra from ground-state hydrogen atoms [6]. We assume the ionizing XUV and streaking IR pulse as linearly polarized along the $z$ axis. The relative time delay between the centers of the two pulses, $\tau$, is assumed positive in case the IR precedes XUV pulse. The electric field $E_X(t)$ of the XUV pulse is characterized by a Gaussian temporal profile, 55 eV central photon energy, and a pulse length of 200 as (FWHIM). The IR pulse has a cosine-squared temporal profile, 720 nm central wavelength, pulse duration of 2 fs FWHIM, and $10^{11}$ W/cm$^2$ peak intensity.

We model streaked photoemission from the ground state of hydrogen, $|\Psi_i\rangle$, based on the quantum-mechanical transition amplitude [6, 28, 51, 55]

$$T(\mathbf{k}_f,\tau) \sim \int dt\ \langle\Psi^{C-V}_{\mathbf{k}_f,\tau}\big|zE_X(t)\big|\Psi_i\rangle, \tag{28}$$

where the IR-pulse-dressed final state of the photoelectron, $\big|\Psi^{C-V}_{\mathbf{k}_f,\tau}\big\rangle$, is a Coulomb-Volkov wavefunction [57] that we evaluate numerically using the ACCTIVE method. In a comparison calculation, we replace the Coulomb-Volkov state by the Volkov state $\big|\Psi^{V}_{\mathbf{k}_f,\tau}\big\rangle$ and assume otherwise identical physical conditions. As mentioned in the Introduction, the use of Volkov states [58] in photoionization calculations is referred to as SFA [6] and amounts to neglecting the interaction of the released photoelectron with the residual ion (proton in the present case). We scrutinize streaked photoemission spectra obtained with ACCTIVE-calculated Coulomb-Volkov final states and in SFA against *ab initio* bench-mark calculations. In these exact numerical calculations we directly solve the three-dimensional TDSE using the SCID-TDSE time-propagation code [74].

Numerical results are shown in Fig. 4. The streaked photoemission spectra obtained with ACCTIVE-calculated Coulomb-Volkov final states [Fig. 4(a)], in SFA [Fig. 4(b)], and by direct numerical solution of the TDSE [Fig. 4(c)] show very similar 'streaking traces', i.e., oscillations of the asymptotic photoelectron energy with delay $\tau$. For a quantitative comparison, we plot in Fig. 4(d) the centers of energy (CoEs) of the spectra in Figs. 4(a-c). While the three calculations result in identical photoemission phase shifts (streaking time delays) relative to the streaking IR field, within the resolution of the graph, the ACCTIVE-calculated spectra agree with the exact TDSE calculation, while the SFA calculation predicts noticeably smaller CoEs due to the neglect of the Coulomb potential in the final photoelectron state [22].

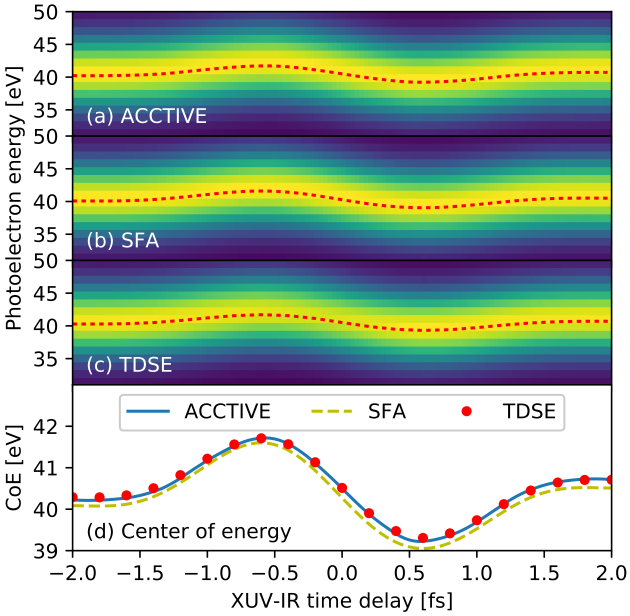

Figure 4. (Color online) IR-streaked XUV photoelectron spectra, (a) based on ACCTIVE-calculated Coulomb-Volkov final states, (b) in SFA, and (c) obtained by direct numerical solution of the TDSE. Red dotted lines in (a-c) indicate the respective centers of energy (CoE). The spectral yields in (a-c) are normalized separately, to their respective maxima. (d) Comparison of the delay-dependent CoE for the spectra in (a-c).

### E. Streaked photoemission from metal nanospheres

As a final, fifth, example, we apply the ACCTIVE method to model photoelectron states in *spatially inhomogeneous*, plasmonically enhanced IR electromagnetic fields. For this purpose, we investigate streaked photoemission [22, 25–27] and the reconstruction of plasmonic near-fields [28] for gold nanospheres with a radius of $R$ = 50 nm. We represent the electronic structure of the nanosphere in terms of eigenstates of a square well with a potential depth of $V_0 = -13.1$ eV and obtain the photoelectron yield by incoherently adding the transition amplitudes (28) over all occupied initial conduction-band states [6, 55, 59]. For the calculation of the transition amplitude (28) we closely follow Ref. [26], with the important difference of employing numerically calculated semiclassical ACCTIVE final photoelectron wavefunctions, while in Ref. [26] the SFA approximation is used, applying heuristically generalized Volkov final states and thus neglecting direct photoelectron interactions with the residual nanoparticle.

For the ACCTIVE calculation we thus solve the

TDSE (1) with the potentials

$$\mathbf{A}(\mathbf{r},t) = \int_t^{\infty} \mathbf{E}_{\mathrm{tot}}(\mathbf{r},t')\, dt' \tag{29a}$$

$$\varphi(\mathbf{r},t) = \begin{cases} V_0 & r < R \\ 0 & r \geq R \end{cases} , \tag{29b}$$

and the boundary condition Eq. (24). Here, the asymptotic wavefunction in Eq. (24) also serves as reference wavefunction for the classical trajectory computation. The net time-dependent inhomogeneous field $\mathbf{E}_{\mathrm{tot}}(\mathbf{r},t)$ is given by the superposition of the homogeneous IR field of the incident streaking pulse and the inhomogeneous plasmonic field produced by the nanoparticle in response to the incident IR pulse [27, 28]. For the streaking calculation, we assume an XUV pulse with 30 eV central photon energy and Gaussian temporal profile with a width of 200 as (FWHIM). We further suppose a delayed Gaussian IR pulse with 720 nm central wavelength, 2.47 fs (FWHIM) pulse length, and $5 \times 10^{10}$ W/cm$^2$ peak intensity.

Figure 5 shows simulated streaked photoelectron spectra obtained with ACCTIVE-calculated and Volkov final states for electron emission along the XUV-pulse polarization direction. In this direction, the effect of the induced plasmonic field on the photoelectron is strongest [28]. The corresponding spectra in Figs. 5(a) and 5(b) show very similar temporal oscillations of the photoelectron yield and CoE as a function of both, asymptotic photoelectron energy and XUV-IR pulse delay $\tau$. As for streaked photoemission from hydrogen atoms discussed in Sec III D above, we find that the SFA shifts the CoE to lower kinetic energies [Fig. 5(b), cf. Fig. 4(d)]. Here, the SFA results in an approximately 1.5 eV lower CoE than the ACCTIVE calculation. This energy shift is due to the fact that the SFA, by neglecting the potential well of the nanosphere in the final photoelectron state, leads to an unphysical enhancement of the photoemission cross section at lower photoelectron kinetic energies, thereby increasing the weight of low energy yields in the CoE average [22]. Addition comments on the comparison of streaked photoelectron spectra within either ACCTIVE or based on Volkov wavefunctions can be found in Appendix D.

From streaked photoemission spectra the plasmonic near-field at the nanoparticle surface can be reconstructed as detailed in Refs. [27, 28]. Figure 5(d) shows the reconstructed net electric field $\mathbf{E}_{\mathrm{tot}}$ along the XUV-pulse polarization direction, i.e., at the surface and on the positive $z$ axis, of the nanosphere. The reconstruction of net plasmonically enhanced near-fields from the simulated spectra in Figs. 5(a) and 5(b) was performed according to the scheme proposed in Ref. [28]. The obtained reconstructed fields are compared in Fig. 5(d) with the net electric IR near-field obtained within Mie theory [75] and used as input in the streaking calculations. As is seen in Fig. 5(d), the ACCTIVE method improves the near-field reconstruction in comparison with the SFA calculation. The least-square deviation between the reconstructed and Mie-theory calculated fields, assembled over the entire IR pulse length, amounts to 1.62% using the ACCTIVE wavefunction and 3.05% using the SFA. A comparative animation of reconstructed and analytical electric fields at the surface of Au nanospheres can be found in the Supplemental Material [73]. The ACCTIVE method thus extends the applicability of the plasmonic near-field reconstruction scheme in Ref. [28] to lower XUV photon energies.

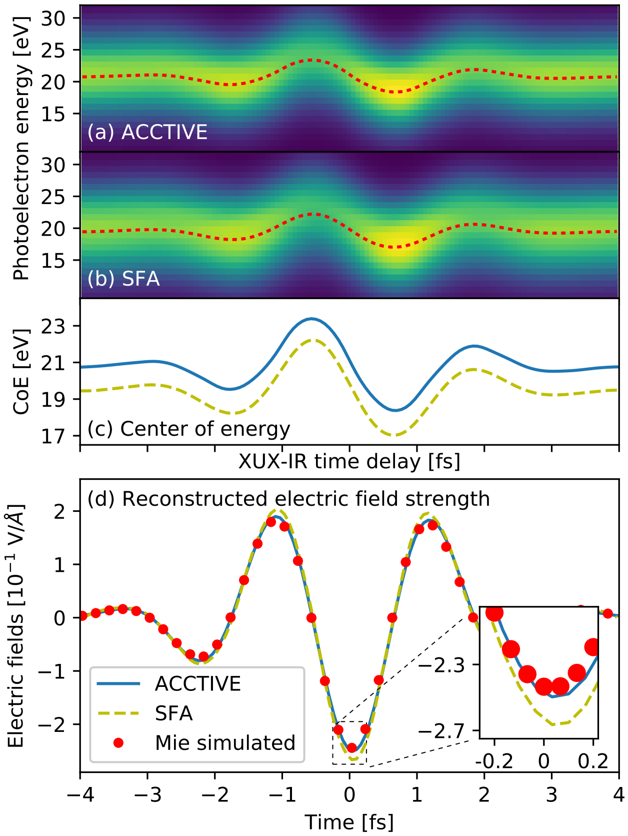

Figure 5. (Color online) Simulated IR-streaked XUV photoelectron spectra for photoemission along the XUV-pulse polarization direction (a) using ACCTIVE final-states and (b) in SFA. (c) Corresponding delay-dependent centers of energy. (d) Comparison of the corresponding reconstructed plasmonic electric near-fields at the point $(x, y, z) = (0, 0, R)$ on the nanoparticle surface with the Mie-theory-calculated electric field.

## IV. SUMMARY

In summary, we propose a semi-classical method, ACCTIVE, to solve the TDSE for one active electron exposed to any spatially inhomogeneous time-dependent external force field. We validate this method by comparing ACCTIVE-calculated electronic wavefunctions with known Coulomb and Volkov wavefunctions for the electronic dynamics in Coulomb and intense laser fields, respectively, and by scrutinizing ACCTIVE-calculated Coulomb-Volkov final photoelectron wavefunctions (i) against *ab initio* numerical solutions of the TDSE and (ii) in streaked photoemission from hydrogen atoms and plasmonic metal nanospheres.

For streaked photoemission from hydrogen atoms, we demonstrate excellent agreement of our ACCTIVE calculation with a benchmark *ab initio* TDSE calculation, while a comparative calculation using the SFA systematically deviates from the exact TDSE solution. For streaked photoemission from Au nanospheres we find that ACCTIVE final-state wavefunctions improve the reconstruction of plasmonic near-fields over SFA calculations (based on Volkov final states) at comparatively low photoelectron energies.

## Appendix A: Gauge invariance of the ACCTIVE method

While Eq. (1) is known to be form invariant under the gauge transformations given by Eqs. (6) [51], we here verify the invariance of Eqs. (4) under the transformations Eqs. (6) and (7).

We first show that the velocity field (9) is gauge invariant. This is easily demonstrated by the following steps,

$$\begin{aligned}\mathbf{p}'(\mathbf{r},t) &\equiv m\mathbf{v}'(\mathbf{r},t)\\ &\equiv \nabla S_0'(\mathbf{r},t) - q\mathbf{A}'(\mathbf{r},t)\\ &= \nabla\Big[S_0(\mathbf{r},t) + qf(\mathbf{r},t)\Big] - q\Big[\mathbf{A}(\mathbf{r},t) + \nabla f(\mathbf{r},t)\Big]\\ &= \nabla S_0(\mathbf{r},t) - q\mathbf{A}(\mathbf{r},t)\\ &\equiv \mathbf{p}(\mathbf{r},t) \equiv m\mathbf{v}(\mathbf{r},t).\end{aligned} \tag{A1}$$

Next, the sequence of identities

$$\begin{aligned}0 &= \frac{\partial}{\partial t}S_0(\mathbf{r},t) + \frac{\big[\nabla S_0(\mathbf{r},t) - q\mathbf{A}(\mathbf{r},t)\big]^2}{2m} + \varphi(\mathbf{r},t)\\ &= \frac{\partial}{\partial t}\Big[S_0'(\mathbf{r},t) - qf(\mathbf{r},t)\Big] + \frac{\big[\nabla S_0'(\mathbf{r},t) - q\mathbf{A}'(\mathbf{r},t)\big]^2}{2m}\\ &\quad + \Big[\varphi'(\mathbf{r},t) + q\frac{\partial}{\partial t}f(\mathbf{r},t)\Big]\\ &= \frac{\partial}{\partial t}S_0'(\mathbf{r},t) + \frac{\big[\nabla S_0'(\mathbf{r},t) - q\mathbf{A}'(\mathbf{r},t)\big]^2}{2m} + \varphi'(\mathbf{r},t)\end{aligned} \tag{A2}$$

proofs the gauge invariance of Eq. (4a). The invariance of the higher order terms in Eqs. (4b) and (4c) is easily recognized by replacing $S_n(\mathbf{r},t)$ with $S_n'(\mathbf{r},t)$ for $n \geq 1$ and $\big[S_0(\mathbf{r},t) - q\mathbf{A}(\mathbf{r},t)\big]$ with $\big[S_0'(\mathbf{r},t) - q\mathbf{A}'(\mathbf{r},t)\big]$.

## Appendix B: Derivation of Eq. (22)

We here derive the Volkov wavefunction Eq. (22) using ACCTIVE. Starting from the potentials and initial wavefunction in Eq. (21), the velocity field along the classical trajectory $\tilde{\mathbf{r}}(t)$ is

$$\mathbf{v}(\mathbf{r},t) = \frac{\mathbf{p}}{m} + \frac{q}{m}\int_{t_0}^{t}\mathbf{E}(t')dt' = \frac{\mathbf{p} - q\mathbf{A}(t)}{m}. \tag{B1}$$

Therefore,

$$\tilde{\mathbf{r}}(t) = \mathbf{r}_0 + \int_{t_0}^{t}\Big[\frac{\mathbf{p} - q\mathbf{A}(t)}{m}\Big]dt', \tag{B2}$$

$$\nabla\cdot\mathbf{v}(\mathbf{r},t) = 0, \tag{B3}$$

and Eq. (19), applied to the example in Sec. III A, becomes

$$\begin{aligned}\Psi(\mathbf{r},t) &= \exp\Bigg\{\frac{i\mathbf{p}\cdot\mathbf{r}_0}{\hbar} + \frac{i}{\hbar}\int_{t_0}^{t}\Bigg[\frac{m}{2}\Big(\frac{\mathbf{p} - q\mathbf{A}(t')}{m}\Big)^2\\ &\qquad + q\Big(\frac{\mathbf{p} - q\mathbf{A}(t')}{m}\Big)\cdot\mathbf{A}(t')\Bigg]dt'\Bigg\}\\ &= \exp\Bigg\{\frac{i\mathbf{p}}{\hbar}\cdot\Bigg[\mathbf{r} - \int_{t_0}^{t}\Big(\frac{\mathbf{p} - q\mathbf{A}(t)}{m}\Big)dt'\Bigg]\\ &\qquad + \frac{i}{\hbar}\int_{t_0}^{t}\Bigg[\frac{m}{2}\Big(\frac{\mathbf{p} - q\mathbf{A}(t')}{m}\Big)^2\\ &\qquad + q\Big(\frac{\mathbf{p} - q\mathbf{A}(t')}{m}\Big)\cdot\mathbf{A}(t')\Bigg]dt'\Bigg\}\\ &= \exp\Bigg\{\frac{i\mathbf{p}\cdot\mathbf{r}}{\hbar} + \frac{i}{\hbar}\int_{t_0}^{t}\Bigg[\frac{m}{2}\Big(\frac{\mathbf{p} - q\mathbf{A}(t')}{m}\Big)^2\\ &\qquad - m\Big(\frac{\mathbf{p} - q\mathbf{A}(t')}{m}\Big)^2\Bigg]dt'\Bigg\}\\ &= \exp\Bigg\{\frac{i\;\mathbf{p}\cdot\mathbf{r}}{\hbar} - \frac{i}{2m\hbar}\int_{t_0}^{t}\big[\mathbf{p} - q\mathbf{A}(t')\big]^2dt'\Bigg\},\end{aligned} \tag{B4}$$

which is the Volkov wavefunction Eq. (22).

## Appendix C: Numerical calculation of Coulomb wavefunctions using ACCTIVE

The ACCTIVE method links a quantum-mechanical problem of obtaining wavefunctions $\Psi(\mathbf{r},t)$ to a classical problem of determining velocity fields $\mathbf{v}(\mathbf{r},t)$. However, in some cases, e.g., for Coulomb wavefunctions, such velocity fields are not uniquely defined (Fig. 6). This can result in interference patterns in the obtained wavefunctions, as pointed out by Goldfarb *et al.* [61].

For each event $(\mathbf{r},t)$, two possible classical trajectories can be found to satisfy the same boundary condition of an outgoing plane wave in Eq. (24), as shown in Fig. 6. Goldfarb *et al.* [61] take this interference into account by

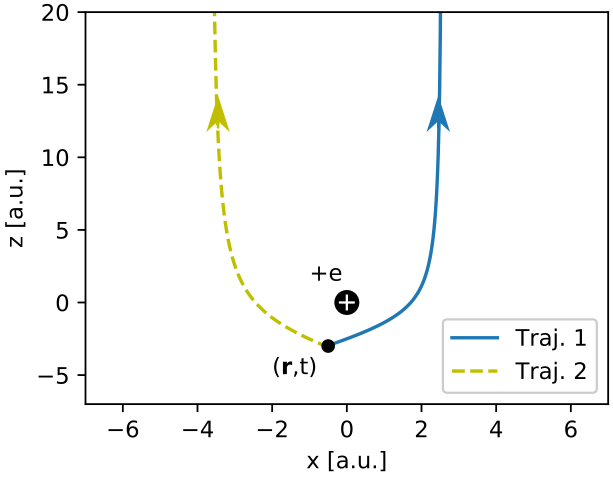

Figure 6. (Color online) Two possible classical trajectories passing through $(\mathbf{r}, t)$ satisfying the same outgoing plane wave boundary condition.

approximating the wavefunction as the superposition of contributions from different trajectories,

$$\Psi(\mathbf{r}, t) \approx \sum_l \exp\left[\frac{i}{\hbar} S^l\left(\tilde{\mathbf{r}}(t), t\right)\right], \tag{C1}$$

where each action $S^l(\mathbf{r}, t)$ is associated with a trajectory $\tilde{\mathbf{r}}^l(t)$. In this work, we follow a different and simpler approach.

The TDSE is a linear partial differential equation. Its solution can be expressed as the superposition of a set of linearly independent basis functions $\Psi^l(\mathbf{r}, t)$,

$$\Psi(\mathbf{r}, t) = \sum_l C^l \Psi^l(\mathbf{r}, t) = \sum_l C^l \exp\left[\frac{i}{\hbar} S^l(\mathbf{r}, t)\right], \tag{C2}$$

where each $S^l(\mathbf{r}, t)$ is uniquely determined by a velocity field $\mathbf{v}^l(\mathbf{r}, t)$ and the coefficients $C^l$ are obtained from the initial condition,

$$\Psi_0(\mathbf{r}) = \sum_l C^l \Psi^l(\mathbf{r}, t_0). \tag{C3}$$

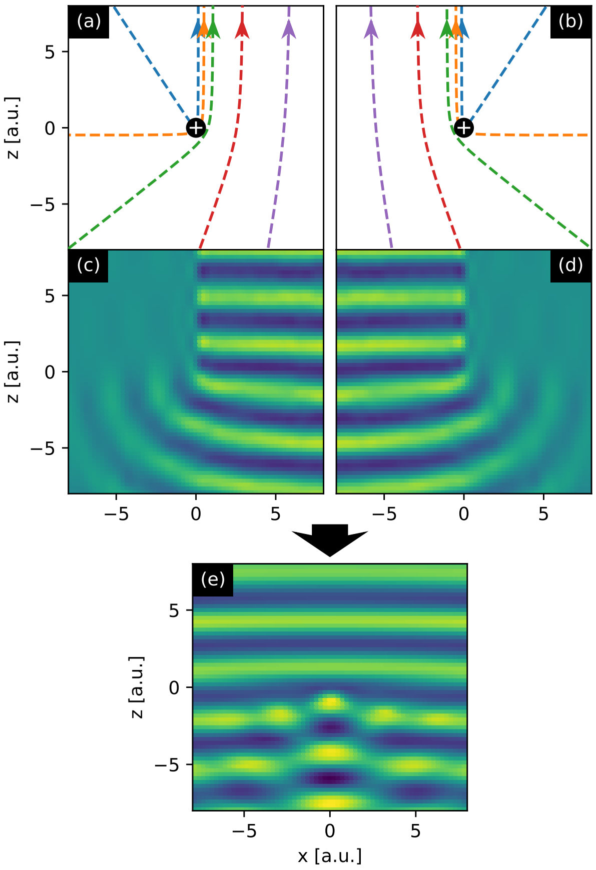

Figure 7. (Color online) Two possible velocity fields (a) $\mathbf{v}^{+}(\mathbf{r}, t)$, and (b) $\mathbf{v}^{-}(\mathbf{r}, t)$. (c) $\Psi^{+}(\mathbf{r}, t)$ and (d) $\Psi^{-}(\mathbf{r}, t)$ are the real parts of the corresponding 1st order ACCTIVE wavefunctions at $y = 0$ plane, respectively, and (d) $\Psi(\mathbf{r}, t)$ is the linear combination of these two wavefunctions.

Since two possible trajectories can be obtained for each given event $(\mathbf{r}, t)$, we can find two velocity fields, $\mathbf{v}^{+}(\mathbf{r}, t)$ and $\mathbf{v}^{-}(\mathbf{r}, t)$, which are defined by

$$\mathbf{v}^{+}(\mathbf{r}, t) \xrightarrow{z \to +\infty,\ x>0} \hat{\mathbf{z}} p/m \tag{C4a}$$

$$\mathbf{v}^{-}(\mathbf{r}, t) \xrightarrow{z \to +\infty,\ x<0} \hat{\mathbf{z}} p/m, \tag{C4b}$$

as illustrated in Fig. 7(a) and 7(b), respectively. Figures 7(c) and 7(d) show the calculated 1st-order ACCTIVE wavefunctions, $\Psi^{+}(\mathbf{r}, t)$ and $\Psi^{-}(\mathbf{r}, t)$, associated with these two velocity fields at $t = 0$. Numerical calculation shows that,

$$\Psi^{+}(\mathbf{r}, t) \xrightarrow{z \to +\infty} \begin{cases} e^{ikz} & x > 0 \\ 0 & x < 0 \end{cases} \tag{C5a}$$

$$\Psi^{-}(\mathbf{r}, t) \xrightarrow{z \to +\infty} \begin{cases} e^{ikz} & x < 0 \\ 0 & x > 0 \end{cases}. \tag{C5b}$$

Therefore, at $t_0$, $\Psi_0(\mathbf{r}) = \Psi(\mathbf{r}, 0)$ can be written as the linear combination of $\Psi^{+}(\mathbf{r}, t_0)$ and $\Psi^{-}(\mathbf{r}, t_0)$ and satisfies the boundary condition (C4),

$$\Psi_0(\mathbf{r}) = \Psi^{+}(\mathbf{r}, t_0) + \Psi^{-}(\mathbf{r}, t_0). \tag{C6}$$

The wavefunction at any given time $t$ is then obtained with the same coefficients,

$$\Psi(\mathbf{r}, t) = \Psi^{+}(\mathbf{r}, t) + \Psi^{-}(\mathbf{r}, t), \tag{C7}$$

as shown in Fig. 7 (e).

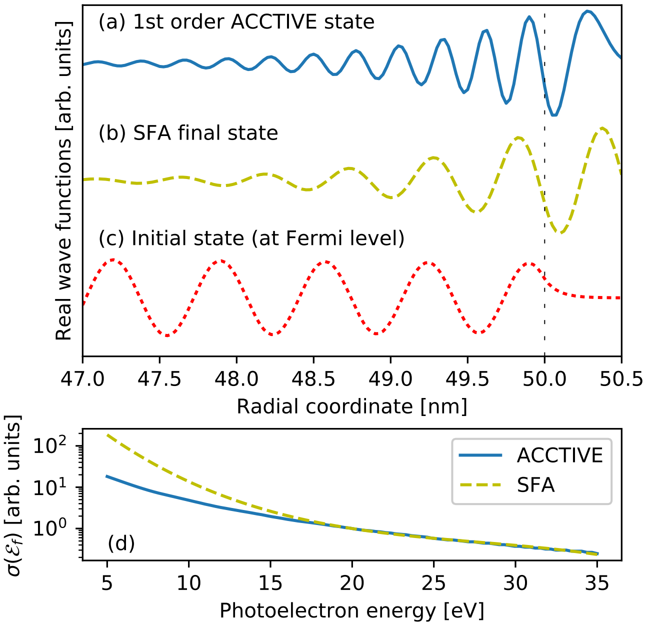

Figure 8. (Color online) Real parts of photoelectron final-state wavefunctions near the surface of Au nanospheres along the XUV polarization direction: (a) 1st order ACCTIVE wavefunction and (b) SFA modeled wavefunction in Ref. [28], for the electron detection along the XUV polarization direction and asymptotic photoelectron energy $\mathcal{E}_f = 5$ eV. (c) Initial-state wavefunction, modeled as bound state in a spherical square well potential, at the Fermi level. The vertical dashed line indicates the nanosphere surface. (d) Simulated XUV photoemission cross sections.

## Appendix D: Comments on streaked photoemission from Au nanospheres

Figure 5 in the main text shows the comparison of simulated streaked photoelectron spectra using either ACCTIVE wavefunctions as final states or Volkov wavefunction in SFA. ACCTIVE wavefunctions are more accurate at low photoelectron energy, but entail higher CoEs than Volkov wavefunctions [Fig. 5(c)]. In comparison with Fig. 4(d), this might appear as counter-intuitive. An explanation is given below.

Figure 8(a) shows the real part of the 1st-order ACCTIVE wavefunction near the Au nanosphere surface, and Fig. 8(b) the corresponding Volkov wavefunction in SFA [28]. Both are calculated for photoelectron detection along the XUV polarization direction and outgoing photoelectron energy $\mathcal{E}_f = 5$ eV. Inside the nanosphere, the Volkov final-state wavefunction neglects the spherical well potential. It therefore has a longer wavelength than the ACCTIVE wavefunction and more strongly overlaps with the initial-state wavefunction shown in Fig. 8(c). Thus, the cross section, calculated following Ref. [51], is larger in SFA than if based on ACCTIVE final states.

This effect becomes less significant a larger photoelectron kinetic energies, where both, ACCTIVE and SFA wavefunctions have shorter wavelengths and overlap less with initial-state wavefunction. Figure 8(d) shows that the energy-dependent photoemission cross sections calculated with ACCTIVE and Volkov final states converge at large photoelectron energies, while at small energies the SFA leads to larger cross sections. The net effect of this cross-section difference is to put more weight on photoelectron yields at lower energy and thus to shift streaking traces and CoEs in SFA photoemission spectra to lower energies as compared to ACCTIVE-calculated spectra.

## ACKNOWLEDGEMENT

This work was supported in part by the Chemical Sciences, Geosciences, and Biosciences Division, Office of Basic Energy Sciences, Office of Science, US Department of Energy under Award DEFG02-86ER13491 (attosecond interferometry), NSF grant no. PHY 1802085 (theory of photoemission from surfaces), and the Air Force Office of Scientific Research award no. FA9550-17-1-0369 (recollision physics at the nanoscale).

[1] S. Hüfner, *Photoelectron Spectroscopy. Principles and Applications* (Springer, Berlin, 2003).
[2] M. Hentschel, R. Kienberger, C. Spielmann, G. A. Reider, N. Milosevic, T. Brabec, P. Corkum, U. Heinzmann, M. Drescher, and F. Krausz, Nature **414**, 509 (2001).
[3] Z. Chang, Phys. Rev. A **70**, 043802 (2004).
[4] G. Sansone, E. Benedetti, F. Calegari, C. Vozzi, L. Avaldi, R. Flammini, L. Poletto, P. Villoresi, C. Altucci, R. Velotta, S. Stagira, S. De Silvestri, and M. Nisoli, Science **314**, 443 (2006).
[5] F. Krausz and M. Ivanov, Rev. Mod. Phys. **81**, 163 (2009).
[6] U. Thumm, Q. Liao, E. M. Bothschafter, F. Süßmann, M. F. Kling, and R. Kienberger, in *The Oxford Handbook of Innovation*, edited by D. Andrew (Wiley, New York, 2015) Chap. 13.
[7] P. M. Paul, E. S. Toma, P. Breger, G. Mullot, F. Augé, P. Balcou, H. G. Muller, and P. Agostini, Science **292**, 1689 (2001).
[8] K. Klünder, J. M. Dahlström, M. Gisselbrecht, T. Fordell, M. Swoboda, D. Guénot, P. Johnsson, J. Caillat, J. Mauritsson, A. Maquet, R. Taïeb, and A. L'Huillier, Phys. Rev. Lett. **106**, 143002 (2011).
[9] R. Locher, L. Castiglioni, M. Lucchini, M. Greif, L. Gallmann, J. Osterwalder, M. Hengsberger, and U. Keller, Optica **2**, 405 (2015).
[10] M. Drescher, M. Hentschel, R. Kienberger, M. Uiberacker, V. Yakovlev, A. Scrinzi, T. Westerwalbesloh,

U. Kleineberg, U. Heinzmann, and F. Krausz, Nature **419**, 803 (2002).

[11] R. Kienberger, E. Goulielmakis, M. Uiberacker, A. Baltuska, V. Yakovlev, F. Bammer, A. Scrinzi, T. Westerwalbesloh, U. Kleineberg, U. Heinzmann, M. Drescher, and F. Krausz, Nature **427**, 817 (2004).

[12] P. Johnsson, J. Mauritsson, T. Remetter, A. L'Huillier, and K. J. Schafer, Phys. Rev. Lett. **99**, 233001 (2007).

[13] H. Wang, M. Chini, S. Chen, C.-H. Zhang, F. He, Y. Cheng, Y. Wu, U. Thumm, and Z. Chang, Phys. Rev. Lett. **105**, 143002 (2010).

[14] M. Schultze, M. Fieß, N. Karpowicz, J. Gagnon, M. Korbman, M. Hofstetter, S. Neppl, A. L. Cavalieri, Y. Komninos, T. Mercouris, C. A. Nicolaides, R. Pazourek, S. Nagele, J. Feist, J. Burgdörfer, A. M. Azzeer, R. Ernstorfer, R. Kienberger, U. Kleineberg, E. Goulielmakis, F. Krausz, and V. S. Yakovlev, Science **328**, 1658 (2010).

[15] C. Ott, A. Kaldun, P. Raith, K. Meyer, M. Laux, J. Evers, C. H. Keitel, C. H. Greene, and T. Pfeifer, Science **340**, 716 (2013).

[16] B. Bernhardt, A. R. Beck, X. Li, E. R. Warrick, M. J. Bell, D. J. Haxton, C. W. McCurdy, D. M. Neumark, and S. R. Leone, Phys. Rev. A **89**, 023408 (2014).

[17] H. Niikura, F. Légaré, R. Hasbani, M. Y. Ivanov, D. M. Villeneuve, and P. B. Corkum, Nature **421**, 826 (2003).

[18] M. F. Kling, C. Siedschlag, A. J. Verhoef, J. I. Khan, M. Schultze, T. Uphues, Y. Ni, M. Uiberacker, M. Drescher, F. Krausz, and M. J. J. Vrakking, Science **312**, 246 (2006).

[19] A. Staudte, D. Pavičić, S. Chelkowski, D. Zeidler, M. Meckel, H. Niikura, M. Schöffler, S. Schössler, B. Ulrich, P. P. Rajeev, T. Weber, T. Jahnke, D. M. Villeneuve, A. D. Bandrauk, C. L. Cocke, P. B. Corkum, and R. Dörner, Phys. Rev. Lett. **98**, 073003 (2007).

[20] S. R. Leone, C. W. McCurdy, J. Burgdörfer, L. S. Cederbaum, Z. Chang, N. Dudovich, J. Feist, C. H. Greene, M. Ivanov, R. Kienberger, U. Keller, M. F. Kling, Z.-H. Loh, T. Pfeifer, A. N. Pfeiffer, R. Santra, K. Schafer, A. Stolow, U. Thumm, and M. J. J. Vrakking, Nat. Photon. **8**, 162 (2014).

[21] B. Förg, J. Schötz, F. Süßmann, M. Förster, M. Krüger, B. Ahn, W. A. Okell, K. Wintersperger, S. Zherebtsov, A. Guggenmos, V. Pervak, A. Kessel, S. A. Trushin, A. M. Azzeer, M. I. Stockman, D. Kim, F. Krausz, P. Hommelhoff, and M. F. Kling, Nat. Commun. **7**, 11717 (2016).

[22] J. Li, E. Saydanzad, and U. Thumm, Phys. Rev. A **94**, 051401 (2016).

[23] L. Seiffert, Q. Liu, S. Zherebtsov, A. Trabattoni, P. Rupp, M. C. Castrovilli, M. Galli, F. Süßmann, K. Wintersperger, J. Stierle, G. Sansone, L. Poletto, F. Frassetto, I. Halfpap, V. Mondes, C. Graf, E. Rühl, F. Krausz, M. Nisoli, T. Fennel, F. Calegari, and M. Kling, Nat. Phys. **13**, 766 (2017).

[24] J. Schötz, B. Förg, M. Förster, W. A. Okell, M. I. Stockman, F. Krausz, P. Hommelhoff, and M. F. Kling, IEEE Journal of Selected Topics in Quantum Electronics **23**, 77 (2017).

[25] E. Saydanzad, J. Li, and U. Thumm, Phys. Rev. A **95**, 053406 (2017).

[26] J. Li, E. Saydanzad, and U. Thumm, Phys. Rev. A **95**, 043423 (2017).

[27] E. Saydanzad, J. Li, and U. Thumm, Phys. Rev. A **98**, 063422 (2018).

[28] J. Li, E. Saydanzad, and U. Thumm, Phys. Rev. Lett. **120**, 223903 (2018).

[29] M. Lucchini, A. Ludwig, L. Kasmi, L. Gallmann, and U. Keller, Opt. Express **23**, 8867 (2015).

[30] C. Chen, Z. Tao, A. Carr, P. Matyba, T. SzilvÃ¡si, S. Emmerich, M. Piecuch, M. Keller, D. Zusin, S. Eich, M. Rollinger, W. You, S. Mathias, U. Thumm, M. Mavrikakis, M. Aeschlimann, P. M. Oppeneer, H. Kapteyn, and M. Murnane, Proc. Natl. Acad. Sci. USA **114**, E5300 (2017).

[31] S. Neppl, R. Ernstorfer, A. L. Cavalieri, C. Lemell, G. Wachter, E. Magerl, E. M. Bothschafter, M. Jobst, M. Hofstetter, U. Kleineberg, J. V. Barth, D. Menzel, J. Burgdörfer, P. Feulner, F. Krausz, and R. Kienberger, Nature **517**, 342 (2015).

[32] Z. Tao, C. Chen, T. Szilvási, M. Keller, M. Mavrikakis, H. Kapteyn, and M. Murnane, Science **353**, 62 (2016).

[33] F. Siek, S. Neb, P. Bartz, M. Hensen, C. Strüber, S. Fiechter, M. Torrent-Sucarrat, V. M. Silkin, E. E. Krasovskii, N. M. Kabachnik, S. Fritzsche, R. D. Muiño, P. M. Echenique, A. K. Kazansky, N. Müller, W. Pfeiffer, and U. Heinzmann, Science **357**, 1274 (2017).

[34] L. Kasmi, M. Lucchini, L. Castiglioni, P. Kliuiev, J. Osterwalder, M. Hengsberger, L. Gallmann, P. Krüger, and U. Keller, Optica **4**, 1492 (2017).

[35] M. J. Ambrosio and U. Thumm, Phys. Rev. A **97**, 043431 (2018).

[36] M. J. Ambrosio and U. Thumm, Phys. Rev. A **100**, 043412 (2019).

[37] M. Ossiander, J. Riemensberger, S. Neppl, M. Mittermair, M. Schäffer, A. Duensing, M. S. Wagner, R. Heider, M. Wurzer, M. Gerl, M. Schnitzenbaumer, J. V. Barth, F. Libisch, C. Lemell, J. Burgdörfer, P. Feulner, and R. Kienberger, Nature **561**, 374 (2018).

[38] C.-H. Zhang and U. Thumm, Phys. Rev. A **84**, 063403 (2011).

[39] S. H. Chew, F. Süßmann, C. Späth, A. Wirth, J. Schmidt, S. Zherebtsov, A. Guggenmos, A. Oelsner, N. Weber, J. Kapaldo, A. Gliserin, M. I. Stockman, M. F. Kling, and U. Kleineberg, Appl. Phys. Lett. **100**, 051904 (2012).

[40] M. Lupetti, J. Hengster, T. Uphues, and A. Scrinzi, Phys. Rev. Lett. **113**, 113903 (2014).

[41] C. Lemke, C. Schneider, T. Leißner, D. Bayer, J. W. Radke, A. Fischer, P. Melchior, A. B. Evlyukhin, B. N. Chichkov, C. Reinhardt, M. Bauer, and M. Aeschlimann, Nano Lett. **13**, 1053 (2013).

[42] Q. Liao and U. Thumm, Phys. Rev. A **92**, 031401 (2015).

[43] A. E. Schlather, A. Manjavacas, A. Lauchner, V. S. Marangoni, C. J. DeSantis, P. Nordlander, and N. J. Halas, J. Phys. Chem. Lett. **8**, 2060 (2017).

[44] M. T. Sheldon, J. van de Groep, A. M. Brown, A. Polman, and H. A. Atwater, Science **346**, 828 (2014).

[45] E. Le Ru and P. Etchegoin, *Principles of Surface-Enhanced Raman Spectroscopy: And Related Plasmonic Effects* (Elsevier, Oxford, 2008).

[46] A. V. Kabashin, P. Evans, S. Pastkovsky, W. Hendren, G. A. Wurtz, R. Atkinson, R. Pollard, V. A. Podolskiy, and A. V. Zayats, Nat. Mater. **8**, 867 (2009).

[47] C. Ayala-Orozco, C. Urban, M. W. Knight, A. S. Urban, O. Neumann, S. W. Bishnoi, S. Mukherjee, A. M. Goodman, H. Charron, T. Mitchell, M. Shea, R. Roy, S. Nanda, R. Schiff, N. J. Halas, and A. Joshi, ACS

Nano **8**, 6372 (2014).
[48] F. Krausz and M. I. Stockman, Nat. Photon. **8**, 205 (2014).
[49] 'Free-Electron Lasers'. A collection of recent articles on FEL generation and characterization and their application in fundamental studies of light-matter interaction. Nature Photonics Collection (January 23, 2019).
[50] J. Duris, S. Li, T. Driver, E. G. Champenois, J. P. MacArthur, A. A. Lutman, Z. Zhang, P. Rosenberger, J. W. Aldrich, R. Coffee, G. Coslovich, F.-J. Decker, J. M. Glownia, G. Hartmann, W. Helml, A. Kamalov, J. Knurr, J. Krzywinski, M.-F. Lin, J. P. Marangos, M. Nantel, A. Natan, J. T. O'Neal, N. Shivaram, P. Walter, A. L. Wang, J. J. Welch, T. J. A. Wolf, J. Z. Xu, M. F. Kling, P. H. Bucksbaum, A. Zholents, Z. Huang, J. P. Cryan, and A. Marinelli, Nat. Photon. (December 2, 2019).
[51] E. Merzbacher, *Quantum Mechanics*, 3rd ed. (Wiley, 1998) pp. 73ff, 115, 315ff, 491, 496.
[52] R. Anzaki, Y. Shinohara, T. Sato, and K. L. Ishikawa, Phys. Rev. A **98**, 063410 (2018).
[53] B. Obreshkov and U. Thumm, Phys. Rev. A **74**, 012901 (2006).
[54] Q. Liao and U. Thumm, Phys. Rev. Lett. **112**, 023602 (2014).
[55] Q. Liao and U. Thumm, Phys. Rev. A **89**, 033849 (2014).
[56] S. Neppl, R. Ernstorfer, A. L. Cavalieri, C. Lemell, G. Wachter, E. Magerl, E. M. Bothschafter, M. Jobst, M. Hofstetter, U. Kleineberg, J. V. Barth, D. Menzel, J. Burgdörfer, P. Feulner, F. Krausz, and R. Kienberger, Nature **517**, 342 (2015).
[57] C.-H. Zhang and U. Thumm, Phys. Rev. A **82**, 043405 (2010).
[58] D. M. Wolkow, Zeitschrift für Physik **94**, 250 (1935).
[59] C.-H. Zhang and U. Thumm, Phys. Rev. Lett. **102**, 123601 (2009).
[60] M. Boiron and M. Lombardi, J. Chem. Phys. **108**, 3431 (1998).
[61] Y. Goldfarb, J. Schiff, and D. J. Tannor, J. Chem. Phys. **128**, 164114 (2008).
[62] W. Becker and Milosevic, Laser Physics **19**, 1621 (2009).
[63] A. D. Bandrauk, F. Fillion-Gourdeau, and E. Lorin, J. Phys. B: At. Mol. Opt. Phys. **46**, 153001 (2013).
[64] H. Goldstein, C. Poole, and J. Safko, *Classical mechanics*, 3rd ed. (Addison-wesley, 2001) pp. 22–23,342,433.
[65] C. G. Broyden, Mathematics of Computation **19**, 577 (1965).
[66] K. E. Atkinson, *An introduction to numerical analysis* (John Wiley & Sons, 2008).
[67] G. K. Batchelor, *An introduction to fluid dynamics* (Cambridge University Press, 1967) p. 74.
[68] L. D. Landau and E. M. Lifshitz, *Quantum mechanics: non-relativistic theory*, 3rd ed. (Elsevier, 1977) p. 570.
[69] L. Rosenberg and F. Zhou, Phys. Rev. A **47**, 2146 (1993).
[70] H. R. Reiss and V. P. Krainov, Phys. Rev. A **50**, R910 (1994).
[71] P. A. Macri, J. E. Miraglia, and M. S. Gravielle, J. Opt. Soc. Am. B **20**, 1801 (2003).
[72] J. Dubois, S. A. Berman, C. Chandre, and T. Uzer, Phys. Rev. A **99**, 053405 (2019).
[73] See Supplemental Material at [url] for animations of the (a) wavefunction comparison and (b) Mie-theory-calculated and reconstructed electric near-field distributions for Au nanospheres.
[74] S. Patchkovskii and H. Muller, Comp. Phys. Commun. **199**, 153 (2016).
[75] G. Mie, Ann. Phys. (Berlin, Ger.) **330**, 377 (1908).